Water Resources Management (2026) 40:426
https://doi.org/10.1007/s11269-026-04786-x

Fully Automated Risk and Hazard Assessment for Decision-support (FARHAD): A Cloud-Native Machine-Learning Framework for Worst-Case Scenario Flood-Risk Mapping via Weakline Analysis

Afshin Fouladi Semnan[1,2] · **Mohammad Javad Ostad Mirza Tehrani**[2]

Received: 27 December 2025 / Accepted: 1 June 2026

Abstract

Practical flood-risk assessment requires methods that represent both baseline flooding and amplification from levees, berms, road embankments, and other discontinuities controlling floodplain connectivity. This study presents FARHAD, a cloud-native machine-learning workflow for weakline-aware flood-risk mapping, demonstrated in two Iranian basins: Aqqala and Poldokhtar. Open geospatial and Earth-observation data were processed in Google Earth Engine to derive terrain, hydrological, hydrographic, land-surface, exposure, and vulnerability predictors. An Extreme Gradient Boosting (XGBoost) depth surrogate was trained against GLOFAS-derived design-event targets to produce 30 m depth rasters for 30-, 100-, 300-, and 1000-year average recurrence intervals. Pixel-wise cross-validation showed high internal agreement, while spatial-block cross-validation indicated more conservative transferability, supporting interpretation as screening-level products rather than independently validated hydraulic simulations. Hazard intensity was characterised using depth and a derived Depth × Velocity proxy, then classified using the Swiss FOEN danger concept and the Australian Disaster Resilience Handbook 7. Hazard layers were combined with gridded population, building footprints, and a composite vulnerability index using Risk = Hazard × Exposure × Vulnerability to generate continuous and classified risk maps. Weaklines were delineated from machine-learning-derived flood extents and terrain context, and closure configurations were ranked using a depth-weighted exposure index. Results show that weakline effects differ by basin morphology. Dense weakline clusters in mountainous Poldokhtar produced corridor-bound increases in upper hazard and risk tiers, whereas selected closures in low-gradient Aqqala generated localised escalation near the urban fringe with limited basin-wide footprint change. FARHAD therefore provides a reproducible screening framework for comparing Baseline and conservative weakline-closure risk patterns in data-scarce catchments.

Keywords Flood-risk mapping · Water resources management · Machine learning · Weakline closure · Vulnerability assessment · Cloud-native hydroinformatics

Extended author information available on the last page of the article

1 Introduction

Flooding remains one of the most damaging natural hazards worldwide, causing loss of life, infrastructure disruption, and major economic impacts (Jonkman 2005). In Iran, repeated flood disasters have affected rural and urban communities, highlighting the need for practical methods that move beyond inundation mapping and identify where flood consequences may concentrate (Rostami et al. 2023; Sharifi and Bokaie 2019). Flood risk emerges when hazard intensity and probability intersect with exposed people, assets, and vulnerability (Merz et al. 2010).

Machine-learning (ML) methods are increasingly used as efficient surrogates for estimating flood depth and extent from terrain, hydroclimatic, and land-surface predictors (Bentivoglio et al. 2022; Mosavi et al. 2018). Recent studies have combined machine learning, geospatial analysis, satellite data, and explainable AI for flood hazard, vulnerability, and risk assessment (Li et al. 2025; Mahmoudnia and Karami 2026; Mishra et al. 2026). Extreme Gradient Boosting (XGBoost) is particularly attractive because it combines strong predictive skill with low computational cost (Chen and Guestrin 2016; Nguyen et al. 2024). However, two limitations remain important. First, many ML-based studies stop at hazard prediction and do not propagate hazard into integrated hazard–exposure–vulnerability (HEV) risk assessment (De Moel et al. 2015). Second, weaklines, including levees, berms, road embankments, and other lateral discontinuities controlling floodplain connectivity, are rarely embedded in quantitative risk mapping (Neal et al. 2015; van Ree et al. 2011; Zhang and Takahashi 2022).

This study introduces FARHAD, an automated flood-risk assessment framework for data-scarce basins. The workflow combines open geospatial and Earth-observation data, an XGBoost flood-depth surrogate, weakline-based closure scenarios, and policy-based risk classification. Flood-depth fields are generated for multiple average recurrence intervals (ARIs) under two scenario modes: a Baseline mode and a conservative weakline-closure envelope. These weakline scenarios are not interpreted as the most likely flood realisations; instead, they represent conservative Worst-Case configurations for identifying locations where structural or geomorphic controls may amplify consequences.

The framework translates flood depth and derived Depth × Velocity (D × V) fields into hazard classes using the Swiss Federal Office for the Environment (FOEN) danger concept and the Australian Disaster Resilience Handbook 7 (ADR7). FOEN emphasises design-event probability and physical intensity (FOCP, 2014; Zimmerman et al. 2005), whereas ADR7 gives stronger emphasis to D × V-based severity and consequence-oriented flood-risk management (AIDR, 2017b; DPE, 2023). Applying both systems to the same hazard, exposure, and vulnerability inputs allows mapped risk patterns to be separated from policy-driven classification differences.

Flood risk is represented as $R = H \times E \times V$ (Crichton 1999; Kron 2005), where hazard (H), exposure (E), and vulnerability (V) are co-registered on a 30 m grid. The resulting risk classes are based on within-basin quantiles and should therefore be interpreted as relative risk tiers, not absolute monetary loss classes or directly transferable thresholds.

The novelty of FARHAD is not the use of XGBoost alone, but the integration of four elements in one reproducible workflow: open-data flood-depth surrogates, weakline-based conservative closure scenarios, a common HEV risk field, and parallel FOEN–ADR7 classification. The framework is demonstrated in Aqqala in the Caspian lowlands and Poldokhtar in the Zagros foothills, representing low-gradient floodplain and confined-valley settings. FARHAD is intended as a transparent screening and decision-support workflow for floodplain planning and infrastructure prioritisation in settings where local hydraulic models, observed water levels, and authoritative flood maps are limited or unavailable.

2 Study Areas and Data

2.1 Study Basins

This study examines two contrasting Iranian basins affected by major flooding in 2019: Aqqala in Golestan Province and Poldokhtar in Lorestan Province. They were selected to test FARHAD across a low-gradient Caspian floodplain and a confined Zagros mountain-valley system. Basin locations and regions of interest (ROIs) used for raster alignment and masking are shown in Figure S1. The 2019 flood information is used only to describe basin context; observed flood depths, surveyed water levels, and official event-reconstruction maps were unavailable for validation.

Aqqala lies within the Gorganrud River catchment in northeastern Iran, draining toward the southeastern Caspian Sea lowlands. It is a low-relief floodplain with extensive agricultural land, wetlands, and clustered rural settlements. During the March 2019 event, intense multi-day rainfall produced widespread ponding, local levee or berm failures (Alborzi et al. 2022; Banizaman 2021), and major village and housing impacts (Tourani and Çağlayan 2021). This setting tests whether weakline closure can amplify flood risk in flat, slow-draining terrain where storage, drainage restriction, and lateral-control features influence inundation persistence.

Poldokhtar is located in the Zagros Mountains of western Iran, where settlements and transport infrastructure are concentrated along narrow river corridors. The basin drains through the Kashkan–Karkheh river system toward the southwestern lowlands and the Persian Gulf drainage basin. The March–April 2019 flood was associated with intense rainfall, very high reported discharges (Miri et al. 2023; Parsian et al. 2021), damaged bridges and roads, and major disruption to highway and railway links (UNDP, 2019). In this confined valley setting, weakline behaviour is expected mainly through abrupt conveyance changes near embankments, bridge approaches, road margins, and levee segments rather than broad floodplain spreading.

Together, the two basins allow FARHAD to be tested across two contrasting weakline settings: storage-dominated amplification in Aqqala and corridor-confined amplification in Poldokhtar.

2.2 Hazard Predictors and Depth Targets

The hazard component was developed from open-access predictor and target rasters used to train and apply the flood-depth surrogate. All datasets were pre-processed in Google Earth Engine (GEE) and Python 3.12, clipped to the basin ROIs, and harmonised to a common 30 m grid. This created a consistent analysis grid but did not add independent hydraulic information beyond the source products. Full details of input rasters, sources, transformations, and resampling procedures are provided in Table S1.

Predictors were grouped into four domains representing the main physical controls on inundation: terrain morphometry, hydrographic proximity and density, land cover and soils, and dynamic hydrologic forcing. Terrain predictors were derived mainly from the SRTMGL1 v3 DEM and included filled elevation (Barnes et al. 2014), slope, plan curvature (Evans 2019; Florinsky 1998), TRASP (Wilson and Gallant 2000), flow accumulation, TWI (Beven and Kirkby 1979; Quinn et al. 1991), and HAND (Quintero et al. 2022). Because SRTM is a surface model rather than a bare-earth LiDAR DEM, residual vegetation and built-structure artefacts may remain, particularly in steep or urbanised areas. Hydrological conditioning reduced local pits and flats but could not fully remove these artefacts.

Hydrographic and infrastructure predictors were derived from OpenStreetMap river and road data, including distance to river, river-network density, and distance to major roads (Borgefors 1986). Distance layers were calculated in projected coordinate systems before final raster alignment for consistency. Land-cover and soil predictors included ESA WorldCover-derived Manning's n, Sentinel-2 NDVI, and Hydrologic Soil Group classes (Arcement and Schneider 1989; Chow 1988; Huete et al. 2002; NRCS, 2009). Manning's n was later combined with predicted depth and local slope to estimate a pixel-scale velocity proxy for Depth × Velocity (D × V) classification; the resulting velocity estimates are screening proxies, not observed or hydraulically calibrated flow velocities. Dynamic forcing was represented by CHIRPS-derived SPI-3 and mean annual rainfall (Funk et al. 2015; McKee et al. 1993).

Flood-depth targets were derived from Copernicus/JRC GLOFAS Flood Hazard v2.1 return-period maps (Dottori et al. 2016, 2022). Native 10–500-year products were used to generate 30-, 100-, 300-, and 1000-year depth fields using pixel-wise Gumbel interpolation/extrapolation (Coles et al. 2001; Johnson et al. 1993). The GLOFAS-derived fields were resampled and aligned to the 30 m analysis grid for consistency with the predictor stack. Accordingly, the XGBoost model is interpreted as spatially redistributing an open-data design-event hazard signal using physiographic predictors, not as producing locally calibrated hydraulic truth. The 1000-year layer is an extrapolated tail estimate beyond the native 500-year product and is treated as more uncertain than lower return periods.

2.3 Risk Component Data

The flood-risk analysis integrates three co-registered components: hazard (H), exposure (E), and vulnerability (V). All layers were prepared on the same 30 m grid and later combined using the multiplicative risk formulation. Operational inputs, scaling rules, and weights are summarised in Table S2.

The hazard component (H) consists of the XGBoost-predicted flood-depth rasters for the 30-, 100-, 300-, and 1000-year ARIs. Pixel-scale velocity proxies were derived from predicted depth, local slope, and Manning's n to calculate Depth × Velocity (D × V) intensities for FOEN and ADR7 classification. The resulting velocity estimates are screening proxies, not measured or hydraulically calibrated velocities.

The exposure component (E) represents people and built assets potentially affected by inundation. Population counts were obtained from WorldPop and converted to persons per 30 m cell (Stevens et al. 2015). Building footprints were obtained from OpenStreetMap (OSM) and rasterised as a binary structural-presence layer. Because OSM building completeness may vary between urban centres and smaller settlements, building exposure is treated as a relative proxy rather than a complete asset inventory.

The vulnerability component (V) represents relative socio-physical susceptibility. It combines VIIRS night-time lights (Elvidge et al. 2013, 2017), built-up intensity (Pesaresi et al. 2013), population density (Stevens et al. 2015), slope, distance to rivers, distance to roads, and building density. Because several indicators partly represent urban intensity, V is treated as a relative screening index rather than a locally calibrated vulnerability model.

All H, E, and V rasters were masked to the basin ROIs, aligned cell-by-cell, and handled consistently for missing values. Hazard varied by ARI, scenario mode, and classification framework, whereas exposure and vulnerability were held fixed to isolate weakline-closure and classification effects.

3 Methods

FARHAD generates pixel-wise flood-risk maps by combining XGBoost-derived design-event flood depths, weakline-based conservative closure scenarios, exposure and vulnerability indices, and FOEN/ADR7 policy classification. Continuous risk is represented as $R = H \times E \times V$, and categorical risk is derived using quantile-based consequence banding. The workflow supports screening and prioritisation in data-scarce basins and does not replace calibrated hydraulic modelling or independent event reconstruction.

The workflow has six stages (Figure S2). First, open-access geospatial datasets are pre-processed into a harmonised 30 m predictor stack. Second, an XGBoost surrogate predicts 30-, 100-, 300-, and 1000-year design-event depths from GLOFAS-derived targets; these outputs are interpreted as open-data hazard surrogates rather than observed or locally calibrated flood-depth fields. Third, candidate weaklines are identified from the near-channel flood boundary and terrain context, and closure scenarios are routed to generate conservative per-ARI hazard envelopes. The 25-year flood extent is used only as an intermediate weakline-screening boundary, not for model training, hazard classification, or risk scoring. Fourth, depth and Depth × Velocity (D × V) fields are classified using FOEN and ADR7 rules. Fifth, hazard, exposure, and vulnerability are combined to produce continuous and categorical risk maps. Finally, diagnostic checks assess model performance, weakline-induced risk migration, velocity-proxy uncertainty, classification sensitivity, and quantile-based robustness. These diagnostics evaluate internal consistency and sensitivity rather than independent event validation. Weakline scenarios are interpreted as conservative screening envelopes, not most-likely flood realisations or probability-weighted failure scenarios.

3.1 Hazard Modelling and Scenario Modes

Flood-depth fields were generated using an Extreme Gradient Boosting (XGBoost) surrogate trained against GLOFAS/LISFLOOD-derived design-event depth targets. XGBoost was selected because ensemble-boosted trees provide high predictive skill and computational efficiency in flood-inundation modelling (Bentivoglio et al. 2022; Chen and Guestrin 2016). Using the predictor stack and target rasters described in Sect. 2.2 and Table S1, the model predicted inundation depth for the 30-, 100-, 300-, and 1000-year ARIs.

Model performance was assessed using pixel-wise and spatial-block five-fold cross-validation (CV) against the GLOFAS-derived target depths. Spatial blocks reduced the influence of spatial autocorrelation and provided a more conservative transferability test. These statistics represent internal surrogate fidelity, not independent event validation. CV results are reported in Table S3.

Each trained model produced per-ARI depth rasters on the hydrologically conditioned 30 m grid. After prediction, depth rasters were checked for return-period monotonicity, so that $D_{30} \leq D_{100} \leq D_{300} \leq D_{1000}$ at each valid pixel. Minor violations were corrected using a cumulative maximum rule across increasing ARIs before hazard classification. A first-flood rule was then used to link depth fields to likelihood: for each pixel, the earliest ARI at which inundation occurs supplied the probability coordinate used in the FOEN and ADR7 matrices.

Hazard classes were assigned independently under FOEN and ADR7. In the FOEN danger concept, water depth and D × V intensity define Low, Medium, and Significant hazard bands, with a Residual category associated with the 1000-year extent (FOCP, 2014; Zimmerman et al. 2005). ADR7 classifies hazards using D × V bands with maximum depth and velocity caps, producing H1–H6 categories from Low to Extreme (AIDR, 2017b; DPE, 2023). Velocity was estimated from predicted depth, local slope, and Manning's n; therefore, D × V-based classes are interpreted as screening classifications rather than calibrated hydraulic velocity products.

Two scenario modes were evaluated. The Baseline mode uses XGBoost-predicted depths without weakline closure. The Worst-Case mode routes single-weakline, cumulative, and selected combined closure configurations for each ARI. Candidate weaklines were derived from the boundary of the 25-year machine-learning-derived flood extent, generated from the same Gumbel-fitted depth family, and intersected with the deeper per-ARI flood extents. The 25-year boundary was used as a near-channel floodplain proxy below the first mapped design event and is consistent with Iranian river-management practice, where the 25-year flood helps define the regulatory riverbed boundary (Khatooni et al. 2023; Panahi et al. 2024).

For each closure scenario, a depth-weighted exposure index was calculated as the sum of depth multiplied by exposure over pixels deeper than 2.0 m. The scenario with the largest value was retained as the conservative Worst-Case scenario for that ARI. The Worst-Case mode therefore produces one selected, spatially coherent closure scenario per ARI rather than a pixel-wise maximum across all scenarios. These maps should be read as conservative screening envelopes, not forecasts of the most probable closure configuration.

3.2 Exposure and Vulnerability Indices

Exposure (E) represents the spatial concentration of people and built assets potentially affected by inundation. WorldPop population counts and rasterised OpenStreetMap (OSM) building footprints were aligned to the 30 m grid, masked to each basin ROI, and normalised to [0, 1]. The exposure index was computed as:

$$E = 0.60\,(Population) + 0.40\,(Buildings) \quad (1)$$

where population and building layers are scaled within each basin. The index was held constant across hazard frameworks and scenario modes, so that differences in risk outputs reflect hazard classification and weakline scenario logic rather than changes in exposure. Exposure counts for depths$\geq$2.0 m were calculated from the native population and building rasters and did not affect the normalised E surface (Stevens et al. 2015). Because OSM building footprints may be incomplete, especially in smaller settlements, the building component is treated as a relative structural-exposure proxy, not a complete asset inventory.

Vulnerability (V) represents relative socio-physical susceptibility. Seven indicators were used: inverted VIIRS-DNB night-time lights (Elvidge et al. 2013, 2017), built-up intensity from GHSL/WorldCover (Pesaresi et al. 2013), WorldPop population density (Stevens et al. 2015), inverted slope, inverted distance to river, inverted distance to roads, and building density. Indicators were scaled to [0, 1] using robust 2nd–98th percentile limits within each basin, with inversions applied where lower raw values indicate greater vulnerability. The composite index was calculated as:

$$V = 0.25(L)^{\downarrow} + 0.20\,(B) + 0.25\,(P) + 0.10(S)^{\downarrow} + 0.10(D_{river})^{\downarrow} + 0.05(D_{road})^{\downarrow} + 0.05\,(B_d) \quad (2)$$

where L is night-time lights, B is built-up intensity, P is population density, S is slope, D_{river} is distance to river, D_{road} is distance to road, B_d is building density, and ↓ denotes inversion after scaling. The weights sum to 1.00 and were adopted as literature-informed screening weights, not locally calibrated vulnerability coefficients (Sharifi and Bokaie 2019; Sherpa and Shirzaei 2022). Because local Iranian depth–damage, post-event loss, or vulnerability-calibration datasets were unavailable, V is interpreted as a relative susceptibility surface, not a parcel-scale vulnerability model or empirical damage function.

3.3 Risk Formulation and Policy Frameworks

The continuous flood-risk surface (R) was calculated as:

$$\mathrm{R} = \mathrm{H} \times \mathrm{E} \times \mathrm{V} \quad (3)$$

where H is the framework-specific hazard intensity score derived from the XGBoost depth and D × V stacks, and E and V are the exposure and vulnerability indices. The multiplicative form was used because high risk emerges where hazard, exposed receptors, and vulnerability co-occur; if any component is low, the composite risk is reduced. R is therefore interpreted as a relative composite risk index, not an expected annual damage or monetary loss model.

The continuous R field was converted into consequence bands using quantile thresholds calculated within each basin and scenario mode. The FOEN-consistent matrix used four consequence bands based on the 25th, 50th, and 75th percentiles, while the ADR7 matrix used five bands based on the 20th, 40th, 60th, and 80th percentiles. The final outputs are risk classes, not consequence classes: Low to Very High for FOEN and Very Low to Extreme for ADR7. These quantile-derived classes are relative within-basin tiers and do not represent absolute monetary loss, direct damage severity, or transferable risk thresholds.

For each pixel, R was assigned to a quantile-based consequence band, the first-flood ARI supplied the probability or likelihood column, and the final risk class was retrieved from the

FOEN-consistent or ADR7 matrix. Because the same E, V, and quantile logic were used for both frameworks, FOEN–ADR7 differences reflect hazard-classification rules and matrix structure rather than alternative exposure or vulnerability inputs.

The FOEN-consistent matrix uses design return period as the probability axis and follows a monotonic probability–consequence logic in which high consequences remain high risk even for rarer design events (Bara 2010; FOCP, 2014). The ADR7 matrix uses equivalent ARI-based likelihood columns and five consequence bands, producing Very Low to Extreme risk classes consistent with ADR Handbook 7 (AIDR, 2017a). The matrix structures are shown in Figure S3. Both matrices are used as policy-translation devices for comparative screening, so FOEN–ADR7 differences are interpreted as policy-driven classification differences rather than empirical damage estimates or statutory classifications.

3.4 Diagnostics and Reproducibility

Diagnostic analyses assessed sensitivity to quantile thresholds, HEV perturbations, weakline scenario selection, classification rules, and Baseline–Worst-Case risk migration. Quantile sensitivity was tested using fixed- and own-banding approaches, while HEV stability was assessed using a $\pm 5\%$ jitter test applied to the Worst-Case risk field. Scenario differences were summarised using $\Delta R = R(W) - R(B)$ maps, where $R(W)$ is the Worst-Case risk surface and $R(B)$ is the Baseline risk surface, together with band-shift rasters and exposure changes above the 2.0 m depth threshold.

Reproducibility was supported by consistent NoData handling, projected-coordinate calculations for distance, area, and density operations, fixed random seeds where supported, and output provenance files. Key adjustable settings, including weights, component-size limits, quantile thresholds, and weakline selection rules, were stored with the outputs.

4 Results

This section presents the main FARHAD outputs for weakline closure, hazard patterns, and risk products under the Baseline and Worst-Case scenario modes and both FOEN and ADR7 frameworks.

4.1 Weakline Inventories and Closure Selection

Composite weakline segments were delineated for Aqqala and Poldokhtar to identify candidate lateral-control features along floodplain margins and river corridors (Figure S4). In Poldokhtar, weaklines form a dense, branching network along both sides of the confined floodplain, with several segments extending toward developed areas. This reflects the valley morphology, where roads, embankments, bridge approaches, and abrupt floodplain edges can influence lateral connectivity. In Aqqala, weaklines are less branched and more concentrated along the eastern and southern floodplain margins. This simpler pattern is consistent with the low-gradient terrain, where floodplain spreading is broader but distinct lateral-control points are more localised. Across both basins, weaklines generally align with the outer boundary of the modelled inundation footprint, indicating potential controls on floodplain expansion rather than confirmed breach locations.

Worst-Case weakline closures were identified for each ARI using the depth-weighted exposure index defined in Sect. 3.1. For each ARI, the closure configuration maximising this index was retained as the conservative Worst-Case scenario. Detailed exposure counts, selected closure sets, and exposure-weighted index values are reported in Table S4, while spatial closure maps are shown in Figures S5 and S6.

Selected closures generally increased depth-weighted exposure relative to the Baseline condition, although responses varied by basin and ARI. In Poldokhtar, closures mainly affected occupied river-corridor areas. Population exposed to depths $\geq$2.0 m ranged from approximately 15,166 people under the 30-year Worst-Case scenario to 22,631 people under the 1000-year scenario. The largest exposure-weighted increase occurred for the 100-year scenario, rising from 116,972 to 184,998, indicating sensitivity to cumulative weakline closure in the confined valley. At higher ARIs, exposed population can decrease locally where closures confine the flood footprint, even when the exposure-weighted index increases because deeper water is concentrated in exposed areas.

In Aqqala, population exposure was lower under the Baseline condition but showed clearer increases under selected closures. Population exposed to depths $\geq$2.0 m increased from 837 to 3,072 under the 30-year scenario and from 6,423 to 11,982 under the 1000-year scenario. This suggests that limited weakline closures can alter ponding patterns in low-gradient terrain.

4.2 Flood-Hazard Patterns

Per-ARI hazard maps were generated from the XGBoost depth fields and classified under FOEN and ADR7. Figure S7 compares the Baseline and Worst-Case hazard products, while Table S5 summarises selected hazard-class area shares. Weakline closures mainly intensified hazards along floodplain margins and near hydraulic constrictions where modelled ponding developed upstream of road and levee segments.

Under FOEN, both depth-based and D × V-based hazard composites were evaluated. In Poldokhtar, the D × V composite produced a slightly larger Significant-hazard footprint than the depth-only composite (3,628 vs. 3,509 pixels). In Aqqala, the contrast was stronger (2,161 vs. 191 pixels). The D × V-based composites were therefore retained for FOEN reporting, indicating that the velocity-proxy intensity term affects the mapped upper hazard footprint, especially in low-gradient floodplain areas.

In Poldokhtar, ADR7 delineates extensive H5–H6 belts along the valley margins and main river corridor, reflecting high D × V-based intensity in the confined valley setting. FOEN identifies similar areas mainly as Significant hazard, with Residual patches near the outer design-event extent. Weakline closures expand selected high-tier belts and infill pockets within the inner floodplain. Under ADR7, H4–H6 area increases from 30.3% in the Baseline scenario to 32.9% in the Worst-Case scenario. Under FOEN, Significant + Residual area increases more modestly, from 26.0% to 26.4%.

In Aqqala, hazard is more broadly distributed across H2–H4 under ADR7 and Medium hazard under FOEN, with high-tier zones concentrated along the right bank and local berms that influence flow exchange with the town. Weakline closures produce localised intensification near the eastern and southern margins rather than basin-wide expansion. Under ADR7, H4–H6 area changes only slightly, from 19.2% to 19.3%. FOEN Significant + Residual area changes from 9.4% to 9.1%, indicating that selected weakline closures mainly redistribute or deepen water within existing inundation areas rather than expanding the high-hazard footprint.

Overall, ADR7 is more responsive to D × V-based intensity changes, especially in confined corridors such as Poldokhtar, whereas FOEN produces smaller areal changes around closure-affected margins. Because exposure and vulnerability are held constant, these hazard-classification differences propagate into the risk results.

4.3 Flood-Risk Patterns

Flood-risk maps were derived using the HEV formulation. For each ARI and scenario mode, a continuous, unitless risk field $R = H \times E \times V$ was computed on the 30 m grid, combining hazard intensity with the exposure and vulnerability indices. Nodata pixels were excluded.

The vulnerability index showed two contrasting patterns: corridor-bound vulnerability in Poldokhtar along the narrow valley floor and river-parallel urban corridor, and broader floodplain vulnerability in Aqqala, where medium-to-high values extended across the town and right-bank settlement areas. These fixed exposure and vulnerability patterns conditioned how Baseline and Worst-Case hazard differences propagated into the risk outputs. Detailed vulnerability surfaces and histograms are provided in Figures S8 and S9.

The continuous risk fields were converted to categorical risk classes using the quantile-banding scheme and first-flood rule described in Sect. 3.3. Figure 1 contrasts the FOEN-consistent and ADR7 risk maps for the Worst-Case layers in both basins. In Poldokhtar, ADR7 depicts broad High–Extreme corridors coinciding with D × V-based intensity, while FOEN concentrates High and Very High classes along closure-affected margins and backwater zones. In Aqqala, both frameworks show a town-wide band of Medium–High risk, with FOEN Very High patches aligned with right-bank closures and ADR7 elevating selected inner-town cells where high hazard overlaps with dense exposure and elevated relative vulnerability.

Urban-focused summaries based on the building mask are provided in Tables S6 and S7. Under FOEN, within-scenario High + Very High shares among classified building-mask pixels changed only modestly from Baseline to Worst-Case in both basins. Under ADR7, the shift toward Extreme classes was slightly stronger in built-up corridors, especially in Poldokhtar, consistent with the framework's sensitivity to D × V-based intensity.

As summarised in Table 1, weakline closures do not strongly expand the total upper-risk area at the basin scale, with changes of $\leq 0.3\%$ points. Instead, they reorganise risk internally, raising local severity under ADR7 and shifting Medium to High or Very High classes under FOEN along closure-affected margins. This indicates that weakline effects act mainly through local amplification and class migration, rather than basin-wide expansion of upper-risk area.

4.4 Sensitivity and Robustness

Pixel-wise cross-validation showed high internal agreement with the GLOFAS-derived targets, with RMSE values of 0.108–0.471 m and mean R^2 values generally above 0.95. Spatial-block cross-validation was more conservative. In Poldokhtar, block-CV RMSE increased to 1.204–1.605 m, with moderate R^2 values of 0.701–0.746. In Aqqala, block-

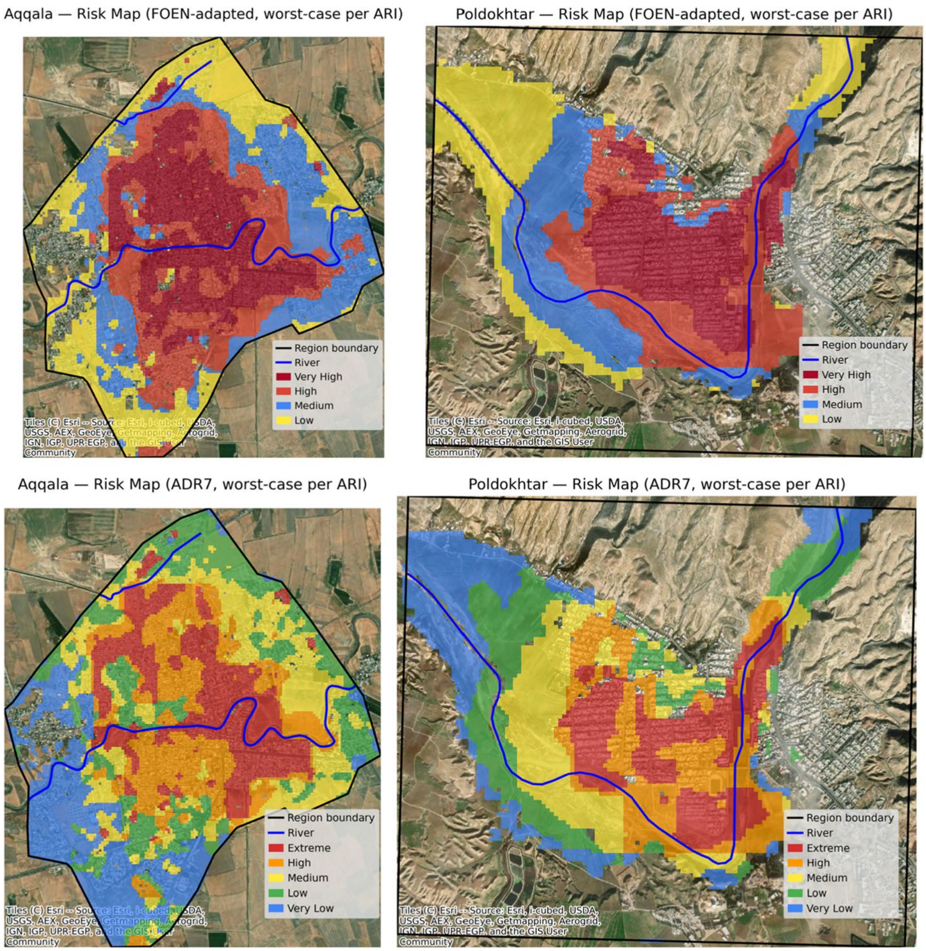

Fig. 1 Flood-risk maps for Worst-Case layers under FOEN and ADR7 frameworks

CV RMSE remained lower at 0.314–0.374 m, but R^2 decreased to 0.169–0.176, reflecting weaker spatial gradients in the low-relief floodplain.

Sensitivity analyses assessed the internal stability of mapped risk changes under quantile thresholds, modest HEV perturbations, and Baseline–Worst-Case spatial differences. FOEN showed limited upward class migration, below 5% in both basins. ADR7 was more sensitive, especially in Aqqala, where upward shifts reached about 9% under own-banding and 7% under fixed-banding. This pattern is consistent with ADR7's stronger dependence on D × V-based hazard intensity. Full migration statistics are provided in Table S8.

The HEV-jitter test applied a spatially varying ± 5% perturbation to the Worst-Case risk field over 20 Monte Carlo realisations. The resulting upper-tier class shares showed negligible variation in both basins (Table S9), indicating stable classification under modest HEV perturbation.

Spatial diagnostics further showed that weakline effects act mainly as local amplifiers. In Poldokhtar, ΔR maps showed compact positive changes along the main river corridor,

Table 1 Upper risk-tier area shares under Baseline and Worst-Case scenarios

Basin	Framework	Upper risk-tier definition	Base-line (%)	Worst-Case (%)	Δ (W–B)	Interpretation
Poldokhtar	FOEN	High + Very High	50.20	50.20	0.00	Upper-risk class share essentially unchanged; closures redistribute intensity within upper tiers
	ADR7	High + Extreme	40.34	40.11	–0.23	Local severity changes without enlarging total upper-risk area
Aqqala	FOEN	High + Very High	50.38	50.53	+ 0.15	Marginal increase; closures deepen flows within the existing footprint
	ADR7	High + Extreme	39.96	40.22	+ 0.26	Minor expansion along closure-affected margins

Note: Δ (W–B) = Worst-Case percentage minus Baseline percentage. Values are basin-area shares from classified risk rasters and represent relative within-basin class shares, not absolute risk or loss estimates

bridge-constriction zones, and urban–valley margins. In Aqqala, positive ΔR appeared as narrow belts along the southern and eastern flow corridors. Across both basins, most pixels remained unchanged or shifted by only one class, while two-class upward shifts were concentrated near closure-sensitive margins (Figures S10 and S11).

Overall, the main high-risk belts persisted across quantile, perturbation, and ΔR tests, while weakline closures mainly reorganised local risk intensity rather than producing unstable basin-wide class changes. These results support FARHAD as a screening and prioritisation workflow.

5 Discussion

FARHAD is best interpreted as a screening-level workflow rather than a calibrated hydraulic model. Its main contribution is not depth prediction alone, but the integration of open-data depth surrogates, weakline scenario testing, HEV risk construction, and parallel FOEN–ADR7 classification within one reproducible framework. This positioning is consistent with recent studies that apply machine-learning and geospatial methods to flood-risk assessment in data-scarce settings and regional-scale hazard–vulnerability screening (Mahmoudnia and Karami 2026; Mishra et al. 2026).

5.1 Spatial and Policy Interpretation

Weakline closures affect modelled flooding differently depending on basin geometry and the arrangement of settlements. In both Aqqala and Poldokhtar, their influence is mainly expressed as lateral redistribution and additional local depth, rather than basin-wide expansion of the inundated area. This supports treating weaklines as potential lateral-control features that modify existing inundation patterns, rather than as independent sources of flooding. Similar behaviour has been reported in hydrodynamic studies where levees, dykes, and embankment controls reshape floodplain storage and ponding, affecting flood-dynamics representation (Burns et al. 2025; Di Baldassarre et al. 2010; Xu et al. 2026).

In Poldokhtar, weaklines are densely grouped along both sides of the valley, so multiple closure scenarios can act together. Backwater ponding, confinement, and reduced lateral connectivity can increase D × V-based intensity along the main urban corridor. The narrow valley geometry amplifies local flow concentration, producing confined high-risk belts that persist across multiple return periods. This corridor-focused amplification is consistent with recent studies of mountainous and semi-confined floodplains, where terrain-constrained urban development and structural controls can concentrate flood risk along valley-floor corridors (Khan et al. 2025; Thapa et al. 2020; Xu and Wang 2026).

In Aqqala, the simpler low-gradient floodplain contains a less branched weakline pattern, but individual closures can have wider spatial influence. Closures along the eastern and southern margins redirected modelled flow toward the urban fringe, generating ponded zones and backwater patterns that locally increased modelled depth without strongly expanding the overall flood footprint. This response is consistent with low-slope basins, where embankments, roads, and human alteration of floodplain surfaces modify the balance between storage and conveyance, shifting hazard severity within an existing footprint rather than creating entirely new inundation zones (Jongman et al. 2015; Rajib et al. 2023).

The FOEN–ADR7 comparison shows that both frameworks identify broadly similar high-risk corridors but translate them through different policy logics. FOEN emphasises design-event probability and physical intensity, producing smoother class transitions across return periods. ADR7 is more responsive to D × V-based severity, making local increases in velocity-proxy intensity more visible in confined reaches. This helps explain the sharper hazard escalation in Poldokhtar's narrow valley and the more muted net response in Aqqala's broader floodplain. The two frameworks should therefore be viewed as complementary interpretations rather than interchangeable classifications.

Taken together, these results show how weakline layers can connect structural discontinuities, levees, embankments, and roads to repeatable patterns of local risk-amplification patterns within FARHAD's screening workflow.

5.2 Limitations and Recommendations

The hazard targets used to train the depth surrogate were derived from Copernicus GLOFAS design-event rasters and interpolated or extrapolated to the adopted ARIs using a Gumbel fit. Although these products are globally consistent and reproducible, they are not event-calibrated local hydraulic simulations. Local mismatches in floodplain storage, conveyance, defence performance, or boundary conditions may therefore persist. The 1000-year layer is more uncertain than the lower ARIs because it is extrapolated beyond the native 500-year GLOFAS product.

Velocity was approximated from depth–slope–roughness relationships and should be interpreted as a screening proxy rather than a calibrated hydraulic velocity field. Exposure data from WorldPop and OSM may contain temporal mismatch and mapping incompleteness, while the vulnerability index uses proxy indicators rather than micro-scale attributes such as floor elevation, building material, storey height, critical-facility function, or household-level vulnerability. Risk tiers were derived from banding of the HEV field and therefore support relative within-basin comparison, not absolute monetary loss, direct damage severity, or transferable risk thresholds.

Weakline-management priorities could target locations where $\Delta R = R(W) - R(B)$ and upward class migration co-locate, such as road and levee margins, bridge approaches, terrace rims, and perimeter embankments that control hydraulic exchange with urban areas. However, these products should support screening and prioritisation rather than replace detailed local hydraulic modelling, engineering inspection, or statutory flood studies.

Future work should link the HEV formulation to observed or hydraulically simulated velocity fields, especially in confined valleys where D × V-based classification is sensitive to velocity assumptions. Coupling the mapped risk tiers with empirical depth–damage curves, dynamic exposure layers, and independent validation data would help move from relative categorical risk toward explicit loss estimation. Weakline detection could be improved through multi-DEM screening and benchmarking against independent flood footprints, post-event impact reports, crowdsourced observations, SAR-derived inundation maps, or simplified breach-growth and hydrodynamic ensembles.

6 Conclusions

This study developed FARHAD, a transparent cloud-native framework for flood-risk mapping that combines open data, machine-learning-based depth prediction, weakline-closure scenarios, and policy-based classification. The XGBoost surrogate reproduced GLOFAS-derived design-event depth targets with high pixel-wise agreement, while spatial-block validation gave more conservative results. These findings support data-driven depth surrogates for flood-risk screening in data-scarce basins, provided that outputs are not interpreted as substitutes for locally calibrated hydraulic models or independent event validation.

Across Aqqala and Poldokhtar, weaklines acted mainly as local amplifiers of flood risk. Conservative closure scenarios increased local depth and Depth × Velocity-based intensity along floodplain margins, bridge constrictions, road embankments, and closure-sensitive corridors, but did not substantially enlarge the basin-wide inundation or risk footprint. These locations represent practical priorities for targeted inspection, mitigation screening, and floodplain management.

Applying FOEN and ADR7 to identical hazard, exposure, and vulnerability inputs showed that mapped risk differences mainly reflect each policy framework's logic. FOEN emphasises design-event probability and physical danger levels, whereas ADR7 gives greater weight to Depth × Velocity-based severity. Both frameworks identified broadly similar high-risk corridors, indicating that basin morphology, exposure, and vulnerability condition the spatial structure of risk, while the chosen framework influences how severity is expressed.

Overall, FARHAD provides a reproducible and policy-transparent workflow for comparing Baseline and conservative weakline-closure risk patterns in data-limited regions. Its main contribution is the integration of open-data depth surrogates, weakline scenario testing, HEV risk construction, and parallel FOEN–ADR7 classification within a single auditable framework. Future work should pair the workflow with observed inundation extents, surveyed water levels, calibrated velocity data, and empirical vulnerability functions to strengthen its use in mitigation, zoning, and resilience planning.

Supplementary Information The online version contains supplementary material available at https://doi.org/10.1007/s11269-026-04786-x.

Acknowledgements The authors gratefully acknowledge the support of the CONNECT Program, the Organisation for Development of International Science and Technology Cooperation of the Presidential Office (ODISTC), and the Centre for International Scientific Studies and Collaborations (CSTID).

Author Contributions Conceptualisation and methodology: Mohammad Javad OSTAD MIRZA TEHRANI; software: Afshin FOULADI SEMNAN; formal analysis: Afshin FOULADI SEMNAN and Mohammad Javad OSTAD MIRZA TEHRANI; investigation: Afshin FOULADI SEMNAN and Mohammad Javad OSTAD MIRZA TEHRANI; validation: Afshin FOULADI SEMNAN and Mohammad Javad OSTAD MIRZA TEHRANI; resources: Afshin FOULADI SEMNAN and Mohammad Javad OSTAD MIRZA TEHRANI; data curation: Afshin FOULADI SEMNAN; writing—original draft preparation: Afshin FOULADI SEMNAN; writing—review and editing: Mohammad Javad OSTAD MIRZA TEHRANI and Afshin FOULADI SEMNAN; visualisation: Afshin FOULADI SEMNAN; supervision: Mohammad Javad OSTAD MIRZA TEHRANI; project administration: Mohammad Javad OSTAD MIRZA TEHRANI; funding acquisition: Mohammad Javad OSTAD MIRZA TEHRANI. All authors have read and approved the final manuscript.

Funding This study was conducted under the ODISTC–KNTU Joint Initiative, CONNECT Program, through the Water Matters Laboratory (WML) postdoctoral fellowship PDV-WML-KNTU-ODISTC-02/23 − 1, supported by grant agreement No. 11502/B-2024 with K. N. Toosi University of Technology (KNTU). The second author was additionally supported in part by the CONNECT Program's Startup Initiation Grant, agreement No. 3297/B-2025, and by the Research Partnership Grant (2023) of the Swiss Leading House South Asia and Iran, Zurich University of Applied Sciences (ZHAW), supported by the State Secretariat for Education, Research, and Innovation (SERI), Switzerland.

Data Availability The source datasets used in this study are openly available from public repositories. The processed outputs, derived products, and implementation materials associated with the SIAVASH and FARHAD frameworks remain the intellectual property of the Water Matters Laboratory (WML), K. N. Toosi University of Technology (KNTU), under grant agreements No. 11502/B-2024 and No. 3297/B-2025. Derived materials may be made available from the corresponding author upon reasonable request, subject to the terms of the relevant grant agreements. Any use of shared materials should cite the present study and acknowledge the Water Matters Laboratory (WML) and the funding sources.

Declarations

Generative AI and AI-Assisted Technologies in the Writing Process During the preparation of this manuscript, the first author used ChatGPT (OpenAI) to support debugging of selected Python scripts, and ChatGPT and Grammarly (Grammarly, Inc.) for language editing, proofreading, and clarity checking. After using these tools, the authors reviewed, edited, and verified the content as needed and take full responsibility for the final manuscript.

Competing Interests The authors declare that they have no competing interests. The funders had no role in the study design; data collection, analysis, or interpretation; manuscript preparation; or the decision to submit the article for publication.

References

AIDR (2017a) Assessing Options and Service Levels for Treating Existing Risk. Retrieved from https://knowledge.aidr.org.au/media/3520/adr-guideline-7-6.pdf

AIDR (2017b) Flood Hazard. Retrieved from https://knowledge.aidr.org.au/media/3518/adr-guideline-7-3.pdf

Alborzi A, Zhao Y, Nazemi A, Mirchi A, Mallakpour I, Moftakhari H, Ashraf S, Izadi R, AghaKouchak A (2022) The tale of three floods: From extreme events and cascades of highs to anthropogenic floods. Weather Clim Extremes 38:100495. https://doi.org/10.1016/j.wace.2022.100495

Arcement G, Schneider V (1989) Guide for selecting Manning's roughness coefficients for natural channels and flood plains. Retrieved from https://pubs.usgs.gov/publication/wsp2339

Banizaman F (2021) An analytical narrative of the spring 2019 flood: Golestan [In Persian]. https://ensafnews.com/288244

Bara C (2010) Factsheet. Social vulnerability to disasters. http://hdl.handle.net/20.500.11850/39091

Barnes R, Lehman C, Mulla D (2014) Priority-flood: An optimal depression-filling and watershed-labeling algorithm for digital elevation models. Comput Geosci 62:117–127. https://doi.org/10.1016/j.cageo.2013.04.024

Bentivoglio R, Isufi E, Jonkman SN, Taormina R (2022) Deep learning methods for flood mapping: a review of existing applications and future research directions. Hydrol Earth Syst Sci 26(16):4345–4378. https://doi.org/10.5194/hess-26-4345-2022

Beven KJ, Kirkby MJ (1979) A physically based, variable contributing area model of basin hydrology/Un modèle à base physique de zone d'appel variable de l'hydrologie du bassin versant. Hydrol Sci J 24(1):43–69. https://doi.org/10.1080/02626667909491834

Borgefors G (1986) Distance transformations in digital images. Comput Vis graphics image Process 34(3):344–371. https://doi.org/10.1016/S0734-189X(86)80047-0

Burns RA, Mulligan RP, Elliott M, van Proosdij D, Murphy E (2025) Numerical modelling of the hydrodynamics driven by tidal flooding of the land surface after dyke breaching. Nature-Based Solutions 7:100218. https://doi.org/10.1016/j.nbsj.2025.100218

Chen T, Guestrin C (2016) XGBoost: A Scalable Tree Boosting System Proceedings of the 22nd ACM SIGKDD International Conference on Knowledge Discovery and Data Mining, San Francisco, California, USA. https://doi.org/10.1145/2939672.2939785

Chow Vt (1988) Open-channel Hydraulics. McGraw-Hill. https://books.google.com/books?id=1r3XAQAACAAJ

Coles S, Bawa J, Trenner L, Dorazio P (2001) An introduction to statistical modeling of extreme values (Vol. 208). Springer. https://doi.org/10.1007/978-1-4471-3675-0

Crichton D (1999) The Risk triangle. In J. Ingleton (Ed.), Natural disaster management (pp. 102–103). Tudor Rose. https://www.ilankelman.org/crichton/1999risktriangle.pdf

De Moel H, Jongman B, Kreibich H, Merz B, Penning-Rowsell E, Ward PJ (2015) Flood risk assessments at different spatial scales. Mitig Adapt Strat Glob Change 20(6):865–890. https://doi.org/10.1007/s11027-015-9654-z

Di Baldassarre G, Montanari A, Lins H, Koutsoyiannis D, Brandimarte L, Blöschl G (2010) Flood fatalities in Africa: From diagnosis to mitigation. Geophys Res Lett 37(22):1–5. https://doi.org/10.1029/2010GL045467

Dottori F, Salamon P, Bianchi A, Alfieri L, Hirpa FA, Feyen L (2016) Development and evaluation of a framework for global flood hazard mapping. Adv Water Resour 94:87–102. https://doi.org/10.1016/j.advwatres.2016.05.002

Dottori F, Alfieri L, Bianchi A, Skoien J, Salamon P (2022) A new dataset of river flood hazard maps for Europe and the Mediterranean Basin. Earth Syst Sci Data 14(4):1549–1569. https://doi.org/10.5194/essd-14-1549-2022

DPE (2023) Flood hazard: Flood risk management guideline FB03. Retrieved from https://www.environment.nsw.gov.au/sites/default/files/flood-risk-management-flood-hazard-230231.pdf

Elvidge CD, Baugh KE, Zhizhin M, Hsu F-C (2013) Why VIIRS data are superior to DMSP for mapping nighttime lights Proceedings of the Asia-Pacific Advanced Network. https://www.researchgate.net/profile/Feng-Chi-Hsu/publication/271020677_Why_VIIRS_data_are_superior_to_DMSP_for_mapping_nighttime_lights/links/561d576608aecade1acb3acd/Why-VIIRS-data-are-superior-to-DMSP-for-mapping-nighttime-lights.pdf

Elvidge CD, Baugh K, Zhizhin M, Hsu FC, Ghosh T (2017) VIIRS night-time lights. Int J Remote Sens 38(21):5860–5879. https://doi.org/10.1080/01431161.2017.1342050

Evans IS (2019) General geomorphometry, derivatives of altitude, and descriptive statistics. In *Spatial analysis in geomorphology* (pp. 17–90). Routledge. https://doi.org/10.4324/9780429273346

Florinsky IV (1998) Accuracy of local topographic variables derived from digital elevation models. Int J Geogr Inf Sci 12(1):47–62. https://doi.org/10.1080/136588198242003

FOCP (2014) Integrated Risk Management: Its importance in protecting people and their livelihoods. Bern, Switzerland: Federal Office for Civil Protection (FOCP) Retrieved from https://www.babs.admin.ch/dam/en/sd-web/zjFzxOAXFCHJ/88_064_Broschuere_Integrales_Risikomanagement-en.pdf

Funk C, Peterson P, Landsfeld M, Pedreros D, Verdin J, Shukla S, Husak G, Rowland J, Harrison L, Hoell A, Michaelsen J (2015) The climate hazards infrared precipitation with stations—a new environmental record for monitoring extremes. Sci Data 2(1):150066. https://doi.org/10.1038/sdata.2015.66

Huete A, Didan K, Miura T, Rodriguez EP, Gao X, Ferreira LG (2002) Overview of the radiometric and biophysical performance of the MODIS vegetation indices. Remote Sens Environ 83(1):195–213. https://doi.org/10.1016/S0034-4257(02)00096-2

Johnson SA, Stedinger JR, Shoemaker CA, Li Y, Tejada-Guibert JA (1993) Numerical Solution of Continuous-State Dynamic Programs Using Linear and Spline Interpolation. Oper Res 41(3):484–500. https://doi.org/10.1287/opre.41.3.484

Jongman B, Winsemius HC, Aerts JC, Coughlan de Perez E, Van Aalst MK, Kron W, Ward PJ (2015) Declining vulnerability to river floods and the global benefits of adaptation. ProceedNatl Acad Sci 112(18):E2271-E2280. https://doi.org/10.1073/pnas.1414439112

Jonkman SN (2005) Global Perspectives on Loss of Human Life Caused by Floods [journal article]. Nat Hazards 34(2):151–175. https://doi.org/10.1007/s11069-004-8891-3

Khan S, Khan AU, Alodah A, Azeem A, Waqas M, Nahas F, Rebouh NY, Youssef YM (2025) Climate-driven flood hazard assessment in data-scarce mountainous basins using a GIS-based machine learning and hydrodynamic modelling under CMIP6 SSP scenarios. Sci Rep 16(1):1800. https://doi.org/10.1038/s41598-025-31390-7

Khatooni K, Hooshyaripor F, MalekMohammadi B, Noori R (2023) A combined qualitative–quantitative fuzzy method for urban flood resilience assessment in Karaj City, Iran. Sci Rep 13(1):241. https://doi.org/10.1038/s41598-023-27377-x

Kron W (2005) Flood Risk = Hazard • Values • Vulnerability [Article]. Water Int 30(1):58–68. https://doi.org/10.1080/02508060508691837

Li Y, Fang Z, Liu J, Lu Z, Zhou H, Yin W, Chen X (2025) A Comparative Study of Urban Pluvial Flood Susceptibility Assessment Based on Multi-Machine Learning Algorithm. Water Resour Manage 40(1):35. https://doi.org/10.1007/s11269-025-04414-0

Mahmoudnia P, Karami J (2026) Flood risk assessment using multitemporal satellite data and explainable artificial intelligence (XAI): Analyzing Susceptibility and Driving Factors. Water Resour Manage 40(8):320. https://doi.org/10.1007/s11269-026-04710-3

McKee TB, Doesken NJ, Kleist J (1993) The relationship of drought frequency and duration to time scales Proceedings of the 8th Conference on Applied Climatology, Anaheim, California. https://climate.colostate.edu/pdfs/relationshipofdroughtfrequency.pdf

Merz B, Hall J, Disse M, Schumann A (2010) Fluvial flood risk management in a changing world. Nat Hazards Earth Syst Sci 10(3):509–527. https://doi.org/10.5194/nhess-10-509-2010

Miri M, Raziei T, Zand M, Kousari MR (2023) Synoptic aspects of two flash flood-inducing heavy rainfalls in southern Iran during 2019–2020. Nat Hazards 115(3):2655–2672. https://doi.org/10.1007/s11069-022-05658-4

Mishra M, Guria R, da Silva RM, Sethi S, Mishra M, Almazroui M, Chakrabortty R, Santos CAG (2026) Integrating Machine Learning and Geospatial Analysis for Flood Hazard, Vulnerability, and Risk Assessment in Odisha, India. Water Resour Manage 40(8):348. https://doi.org/10.1007/s11269-026-04709-w

Mosavi A, Ozturk P, Chau K-w (2018) Flood prediction using machine learning models. Literature Rev Water 10(11):1536. https://doi.org/10.3390/w10111536

Neal JC, Odoni NA, Trigg MA, Freer JE, Garcia-Pintado J, Mason DC, Wood M, Bates PD (2015) Efficient incorporation of channel cross-section geometry uncertainty into regional and global scale flood inundation models. J Hydrol 529:169–183. https://doi.org/10.1016/j.jhydrol.2015.07.026

Nguyen HD, Dang DK, Nguyen NY, Van P, Van Nguyen C, Nguyen TT, Nguyen Q-H, Pham XL, Pham LT, V. T., Bui Q-T (2024) Integration of machine learning and hydrodynamic modeling to solve the extrapolation problem in flood depth estimation. J Water Clim Change 15(1):284–304. https://doi.org/10.2166/wcc.2023.573

NRCS (2009) Chapter 7: Hydrologic Soil Groups. In Natural Resources Conservation Service (Ed.), National Engineering Handbook (Part 630: Hydrology ed.). United States Department of Agriculture. https://directives.nrcs.usda.gov/sites/default/files2/1712930597/11905.pdf

Panahi G, Khodashenas SR, Faridhosseini A (2024) Using geomorphologic indicators in preparation for flood zoning and flood risk maps in the Kashafroud basin, Iran. J Flood Risk Manag 17(2):e12981. https://doi.org/10.1111/jfr3.12981

Parsian S, Amani M, Moghimi A, Ghorbanian A, Mahdavi S (2021) Flood Hazard Mapping Using Fuzzy Logic, Analytical Hierarchy Process, and Multi-Source Geospatial Datasets. Remote Sens 13(23):4761. https://www.mdpi.com/2072-4292/13/23/4761

Pesaresi M, Huadong G, Blaes X, Ehrlich D, Ferri S, Gueguen L, Halkia M, Kauffmann M, Kemper T, Lu L, Marin-Herrera MA, Ouzounis GK, Scavazzon M, Soille P, Syrris V, Zanchetta L (2013) A Global Human Settlement Layer From Optical HR/VHR RS Data: Concept and First Results. IEEE J Sel Top Appl Earth Observations Remote Sens 6(5):2102–2131. https://doi.org/10.1109/jstars.2013.2271445

Quinn P, Beven K, Chevallier P, Planchon O (1991) The prediction of hillslope flow paths for distributed hydrological modelling using digital terrain models. Hydrol Process 5(1):59–79. https://doi.org/10.1002/hyp.3360050106

Quintero F, Li Z, Demir I, Grout T, Bates B (2022, 19–24 June) Understanding the Mechanisms Behind the Performance of HAND Flood Inundation Model Frontiers in Hydrology 2022, San Juan, Puerto Rico. https://ui.adsabs.harvard.edu/abs/2022frhy.conf11304Q/abstract

Rajib A, Zheng Q, Lane CR, Golden HE, Christensen JR, Isibor II, Johnson K (2023) Human alterations of the global floodplains 1992–2019. Sci Data 10(1):499. https://doi.org/10.1038/s41597-023-02382-x

Rostami Y, Ostad MirzaTehrani MJ, Alizad K, Falahat H (2023) Flood assessment for sustainable development: a case study of bandar abbas, Iran proceedings of the 40th IAHR World Congress, Vienna, Austria. https://doi.org/10.3850/978-90-833476-1-5_iahr40wc-p1651-cd

Sharifi L, Bokaie S (2019) Priorities in prevention and control of flood hazards in Iran 2019 massive flood. Iran J Microbiol 11(2):80–84. https://pmc.ncbi.nlm.nih.gov/articles/PMC6635305/

Sherpa SF, Shirzaei M (2022) Country-wide flood exposure analysis using Sentinel-1 synthetic aperture radar data: Case study of 2019 Iran flood. J Flood Risk Manag 15(1):e12770. https://doi.org/10.1111/jfr3.12770

Stevens FR, Gaughan AE, Linard C, Tatem AJ (2015) Disaggregating census data for population mapping using random forests with remotely-sensed and ancillary data. PLoS ONE 10(2):e0107042. https://doi.org/10.1371/journal.pone.0107042

Thapa S, Shrestha A, Lamichhane S, Adhikari R, Gautam D (2020) Catchment-scale flood hazard mapping and flood vulnerability analysis of residential buildings: The case of Khando River in eastern Nepal. J Hydrology: Reg Stud 30:100704. https://doi.org/10.1016/j.ejrh.2020.100704

Tourani M, Çağlayan A (2021) Example of the biggest flood disaster in Iranian history: Golestan province (NE Iran). Geoscience for Society, Education and Environment. https://appliedgeophysics.ro/wp-content/uploads/2020/12/1.2.GEOSCIENCE_FOR_SOCIETY_Tourani-et-al.pdf

UNDP (2019) Post Disaster Needs Assessment (PDNA): Iran 2019 Floods in Lorestan, Khuzestan and Golestan Provinces. In U. N. D. Programme (Ed.). https://www.undp.org/iran

van Ree CCDF, Van MA, Heilemann K, Morris MW, Royet P, Zevenbergen C (2011) FloodProBE: technologies for improved safety of the built environment in relation to flood events. Environ Sci Policy 14(7):874–883. https://doi.org/10.1016/j.envsci.2011.03.010

Wilson JP, Gallant JC (2000) Terrain Analysis: Principles and Applications. Wiley. https://books.google.com/books?id=1311_4-zvy4C

Xu Y, Wang X (2026) Mountainous urban development unintentionally reshapes spatial patterns of flood disaster risk. Int J Disaster Risk Reduct 141:106206. https://doi.org/10.1016/j.ijdrr.2026.106206

Xu S, Sun H, Zhang L, Han J, Pan R, Yang L, Xiang X, Tang L (2026) Compound effects of dams and levees reshape Yangtze flood dynamics and reveal substantial risk misestimations from ignoring levees. Sci Rep 16(1). https://doi.org/10.1038/s41598-026-41694-x

Zhang W, Takahashi A (2022) Statistical and Parametric Studies on Natural Levees as Weak Points Against Leakages in River Levees. Geotech Geol Eng 40(11):5643–5666. https://doi.org/10.1007/s10706-022-02238-y

Zimmerman M, Pozzi A, Stoessel F (2005) VADEMECUM: Hazard Maps and related Instruments - The Swiss System and its Application abroad. Retrieved from https://www.shareweb.ch/site/DRR/Documents/Types%20of%20activity/Risk%20Assessments/Vademecum_Hazard%20map_PLANAT_2005.pdf

Authors and Affiliations

Afshin Fouladi Semnan[1,2] · **Mohammad Javad Ostad Mirza Tehrani**[2]

✉ Mohammad Javad Ostad Mirza Tehrani
mohammad.tehrani@kntu.ac.ir

[1] Civil and Infrastructure Engineering Discipline, STEM College, RMIT University, Melbourne, VIC 3000, Australia

[2] Water Matters Laboratory (WML), Water Chair, Faculty of Civil Engineering, K. N. Toosi University of Technology (KNTU), Tehran, Iran